ADVANCED FUNCTIONAL MATERIALS
www.afm-journal.de

www.MaterialsViews.com

FULL PAPER

Superparamagnetic Liposomes for MRI Monitoring and External Magnetic Field-Induced Selective Targeting of Malignant Brain Tumors

*Hélène Marie, Laurent Lemaire, Florence Franconi, Sonia Lajnef, Yves-Michel Frapart, Valérie Nicolas, Ghislaine Frébourg, Michael Trichet, Christine Ménager, and Sylviane Lesieur**

Magnetic-fluid-loadedliposomes (MFLs) of optimized magnetic responsiveness are newly worked out from the entrapment of superparamagnetic maghemite nanocrystals in submicronic PEG-ylated rhodamine-labelled phospholipid vesicles. This nanoplatform provides an efficient tool for the selective magnetic targeting of malignant tumors localized in brain and non-invasive traceability by MRI through intravascular administration. As assessed by in vivo 7-T MRI and ex vivo electron spin resonance, 4-h exposure to 190-T m^{-1} magnetic field gradient efficiently concentrates MFLs into human U87 glioblastoma implanted in the striatum of mice. The magnetoliposomes are then longer retained therein as checked by MRI monitoring over a 24-h period. Histological analysis by confocal fluorescence microscopy confirms the significantly boosted accumulation of MFLs in the malignant tissue up to the intracellular level. Electron transmission microscopy reveals effective internalization by endothelial and glioblastoma cells of the magnetically conveyed MFLs as preserved vesicle structures. The magnetic field gradient emphasizes MFL distribution solely in the tumors according to the enhanced permeability and retention (EPR) effect while comparatively very low amounts are recovered in the other cerebral areas. Such a selective targeting precisely traceable by MRI is promising for therapeutic applications since the healthy brain tissue can be expected to be spared during treatments by deleterious anticancer drugs carried by magnetically guided MFLs.

1. Introduction

Specific delivery of therapeutic molecules and/or imaging agents to a pathological site is one of the major challenges in the pharmaceutical sciences field. The goal is to bring and sustain efficient amounts of the active substance to the diseased place while sparing the healthy tissue thereby minimizing potential side effects. Specific delivery is a key problem in cancer therapy due to often nonrestricted cytotoxicity of chemotherapeutics and the need of early diagnosis through selective localization of malignant neoplasms. This is especially tricky in the case of brain which is a particularly delicate vital organ. The difficulty of treatment mainly arises from the diffuse behavior and heterogeneous invasiveness of brain tumors which usually impede complete resection or even prevent any surgical intervention as this may cause severe damages in the healthy brain. At this stage, although radiotherapy and adjuvant systemic administration of antineoplasic molecules improve overall survival, the risk of relapse is unfortunately inevitable. Beyond the own efficacy

---

Dr. H. Marie, Dr. S. Lesieur
Laboratoire Physico-Chimie des Systèmes Polyphasés
Institut Galien Paris-Sud, UMR CNRS 8612
Faculté de Pharmacie, Université Paris-Sud,
LabEx LERMIT, 5 rue Jean-Baptiste Clément
Châtenay-Malabry Cedex, 92296, France
E-mail: sylviane.lesieur@u-psud.fr

Dr. L. Lemaire
INSERM UMR-S 1066, Micro et Nanomédecines Biomimétiques – MINT
Université d'Angers, LUNAM Université
4 rue Larrey, Angers 49933, France

Dr. F. Franconi
PRIMEX-CIFAB, LUNAM Université, Université d'Angers
IRIS/IBS, CHU d'Angers
4 rue Larrey, Angers 49933, France

S. Lajnef, Dr. Y.-M. Frapart
UMR CNRS 8601, FR3443
Université Paris Descartes – Sorbone Paris Cité,
45 rue des Saints Pères
Paris Cedex 06, 75270, France

V. Nicolas
Plateforme Imagerie cellulaire, IFR 141-IPSIT
Faculté de Pharmacie, Université Paris-Sud
5 rue Jean-Baptiste Clément
Châtenay-Malabry Cedex, 92296, France

Dr. M. Trichet, G. Frébourg
Institut de Biologie Paris-Seine, service de microscopie électronique
Université Pierre et Marie Curie
9 Quai Saint Bernard, Paris 75005, France

Prof. C. Ménager
Equipe Colloïdes Inorganiques, Phenix, UMR CNRS 8234
Université Pierre et Marie Curie – Paris 6
4 place Jussieu, Paris Cedex 05, 75252, France

DOI: 10.1002/adfm.201402289

of chemotherapeutics, the exceptional endogenous protection of the brain strongly limits their accessibility to the malignant cells. However, most trials to enhance intratumor distribution of conventional dosage forms do not spare the healthy cerebral tissue and then cause occasionally inacceptable neurotoxic side effects.[1]

The inefficacy of chemotherapeutics to treat brain diseases has been traditionally attributed to the presence of the blood–brain barrier (BBB). This mainly consists of contiguous endothelial cells with intercellular tight junctions, a lack of fenestrations and low pinocytosis, which restrict the entry of many circulating blood constituents including therapeutics.[2,3] Strategies like osmotic disruption,[1] conversion of the active molecules into either lipophilic prodrugs[4] or substrates of transport proteins expressed on the surface of the endothelial cells[5] have been attempted to circumvent BBB, however with no effective distinction between healthy and diseased tissues. In the special case of malignant neoplasms, a more specific approach of delivery has been considered which relies on BBB alteration within the tumor, namely the loss of the tight junctions and the presence of fenestrations, significantly enhancing the vasculature permeability.[6–9] Thereby, passive targeting towards gliomas of intravenously administered colloidal systems with sizes indeed too large to cross healthy BBB, has been assessed in animal models.[10–13] Selective accumulation in the tumor interstitium has been rightly attributed to the so-called enhanced permeability and retention (EPR) effect, widely underscored for malignant neoplasms occurring in other organs.[14] To strengthen EPR effect and ultimately reduce the injection doses, complementary targeting strategies have been developed and adapted to various nanoscale delivery carriers. Active targeting involving biochemical processes of specific recognition of cerebral tumor cells and effected by the conjugation of site-specific ligands to the nanocarriers, has been deeply investigated.[15] The main demonstrated improvement provided by biochemical targeting is to promote highly selective delivery of imaging agents or anti-cancer drugs to glioma cells once they have reached the tumor interstitium through passive EPR effect.[16–21]

The alternative approach envisaged here consists in the application of an external magnetic field gradient to the tumor site in order to therein accumulate magnetically responsive nanoscale systems. The feasibility of magnetic targeting towards gliomas, in a selective way attributed to the abnormalities of the tumor vasculature, has been established for individual magnetic solid particles stabilized by a biocompatible polysaccharide-based shell.[22–24] To date, this has been never transposed to the magnetically responsive nanoscale reservoirs referred to as magnetoliposomes, indeed capable of entrapping and convey guest therapeutics to malignant tissues through intravascular route.[25–27] The present work deals with the ability of specially designed magnetic-fluid-loaded liposomes (MFLs) to be concentrated in malignant brain tumors by the action of a magnetic field gradient. This hybrid system prepared in isotonic pH 7.4 aqueous buffer, consists of a suspension of superparamagnetic citrate-stabilized maghemite nanocrystals encapsulated in the inner cavity of 200-nm sized phosphatidylcholine vesicles coated by poly(ethylene glycol) (PEG) chains. MFLs fulfill the prerequisites for in vivo magnetic targeting applications. They are namely biocompatible, biodegradable, and nontoxic while the confinement of the contained iron oxide nanocrystals makes them efficient T_2 MRI contrast agents, provided with high magnetophoretic ability.[28] PEG coating ensures a long-circulating behavior of MFLs as intact structures with a plasmatic half-life close to 12 h.[29] This has been used to magnetically target intravessel injected MFLs towards human prostatic adenocarcinoma or breast-cancer tumors, subcutaneously xenografted in mice[30–33] whereas magnetically driven intracellular accumulation has been shown in cellulo and in vivo.[34,35] In these previous approaches, the magnetic field source was positioned in the very close vicinity of the tumors or cells. In the present work, the magnetic responsiveness of MFLs was significantly improved by subjecting them to selective magnetic sorting in order to successfully target one of the most frequent and aggressive malignant tumor of the central nervous system, glioblastoma multiforme (GBM), a grade IV glioma that primarily develops in the cerebral hemispheres.[36–38] GBM targeting was assessed in vivo on an orthotopically implanted intracerebral model of human glioblastoma U87 in nude mice, aptly more relevant than tumors resulting from heterotopic subcutaneous inoculation. Experiments were implemented to highlight the efficiency of a magnetic field gradient of 190-T m^{-1} produced by a 0.4-T permanent magnet externally placed on the head of the animals, to selectively concentrate the liposome structures in the malignant neoplasm beside healthy brain. In vivo tracking of MFLs in brain was performed by quantitative MRI. Ex vivo electron spin resonance (ESR) spectroscopy was used to amount the iron oxide delivered in healthy parenchyma and tumor tissue, respectively. ESR analysis provided insight in overall MFLs biodistribution. Detailed histological investigation to approach the mechanism of targeting undergone by the magnetic nanocarriers was carried out on one hand by confocal fluorescence microscopy to reveal the location of the vesicle structures and on the other hand, by electron microscopy to examine the fate of MFLs at the cellular scale. The results together aimed at accurately depicting the traffic of the magnetoliposomes and determining whether the integrity of their structure could be affected or not upon their passage from brain vasculature towards the tumor interstitium, and finally at defining to what extent the healthy parts of the brain can be preserved from magnetic driving of MFLs.

2. Results

2.1. Magnetoliposome Characterization

Rhodamine-labeled magnetic-fluid-loaded PEG-ylated liposomes (MFLs) were thoroughly prepared in isotonic buffer by sequential extrusion followed by flash SEC-purification.[28,32,39] Magnetic sorting was then newly implemented to select MFLs with a number of encapsulated magnetic particles effectively responsive to the magnetic force exerted by the magnets which were used for the in vivo experiments. According to QELS analysis, the resulting magnetoliposomes showed unimodal size distribution with a z-average hydrodynamic diameter of 212 ± 29 nm while the maghemite (γ-Fe_2O_3) nanoscale crystals forming the entrapped magnetic fluid were characterized by a mean

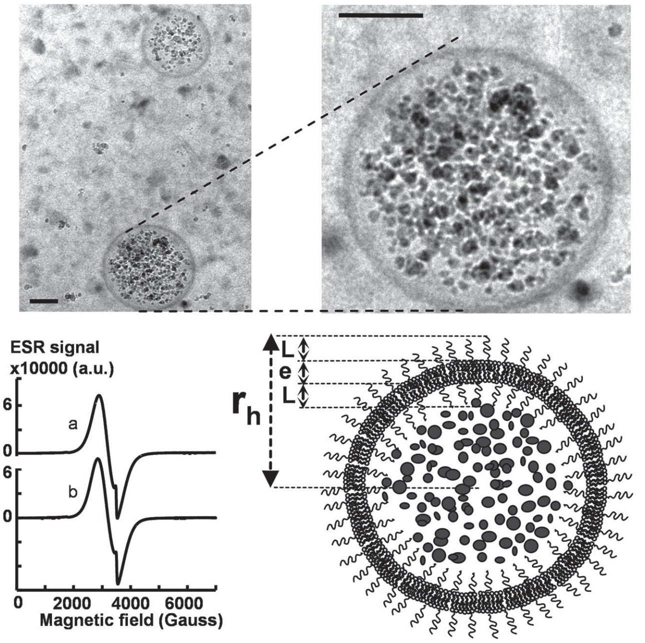

Figure 1. Cryo-TEM images (top) of the magnetic-fluid-loaded liposomes (MFLs) synthesized in this study (iron oxide loading: 4.4 ± 0.5 moles Fe(III) per mole of total lipids); black bars represent 100 nm. Schematic MFL structure (bottom right): r_h corresponds to the liposome hydrodynamic diameter, L to the length of the PEG brush coating and e to the lipid bilayer thickness. The inner vesicle aqueous volume accessible to the maghemite particles is given by $4\pi/3\ (r_h - 2L - e)^3$ with reasonable estimates of the two latter parameters from literature data: $L = 50$ Å[40,41] and $e = 40$ Å.[44,45] Typical X-band at 9.2 GHz resonance frequency of second-derivative ESR spectra (bottom left) of (a) maghemite nanocrystals in free aqueous suspension (1 µL at [Fe(III)] = $57 \pm 2 \times 10^{-3}$ M, 57 Iron(III) nanomoles) and of b) MFLs at equivalent Fe(III) concentration (1 µL at [Fe(III)] = $64 \pm 3 \times 10^{-3}$ M, and $[\text{Lip}]_{\text{tot}} = 14.7 \times 10^{-3}$ M, 64 Iron(III) nanomoles).

hydrodynamic diameter of 13.3 ± 3.5 nm from number distribution. The cryogenic transmission electron microscopy (cryo-TEM) picture in **Figure 1** exemplifies the typical structure of MFLs which consists of one single lipid bilayer enclosing individualized maghemite nanoparticles not interacting with the vesicle membrane and having sizes predominantly in the 5–10 nm range, in agreement with the average grain diameter close to 8 nm deduced from the magnetization curve. The slight shift compared with QELS size arises from the fact that the hydrodynamic diameter takes into account the hydration water bound to the citrate-anion coating and driven by the particles in movement. The total iron oxide loading (Q) determined by atomic absorption spectroscopy was found equal to 4.4 ± 0.5 moles of Fe(III) per mole of total lipids. The size characteristics and encapsulation rate of so-obtained MFLs were both highly stable for 6 months at least. An estimate of the inner iron oxide concentration in the liposomes ($[\text{Fe(III)}]_{\text{inner}}$) can be calculated from the Q value and the fraction of the aqueous volume entrapped by MFLs and accessible to the maghemite particles, according to the following relationship:

$$[Fe(III)]_{\text{inner}} = \frac{Q\,N_{\text{ag}}}{N\dfrac{4\pi}{3}(r_{\text{h}} - 2L - e)^3} \tag{1}$$

N_{ag} is the number of lipid molecules forming the vesicle bilayer (vesicle aggregation number), r_{h} the mean hydrodynamic radius of MFLs, L the thickness of the poly(ethylene glycol) coating (length of PEG chains in brush conformation,[40–43] and e the thickness of the vesicle bilayer. Reasonable values of parameters L and e are given in the legend of Figure 1. The aggregation number N_{ag} can be deduced from the ratio of the bilayer volume per vesicle to the molecular volume of the lipids embedded in the bilayer (V_{m}):

$$N_{\text{ag}} = \frac{4}{3}\pi\left(r_{\text{h}}^3 - (r_{\text{h}} - 2L - e)^3\right)/V_{\text{m}} \tag{2}$$

By taking $V_{\text{m}} = 1264$ Å^3 as the average of the phospholipid molecular volume reported in the literature (Small[44] and Petrache,[45] and $r_{\text{h}} = 1060$ Å, Equations (1) and (2) assessed a mean intraliposome concentration of magnetic material $[\text{Fe(III)}]_{\text{inner}}$ of 3.1 ± 0.6 mol L^{-1}. On the basis of an iron composition of the maghemite particles equivalent to 38 iron atoms per nm^3,[46] this local concentration leads to an estimate of the average number of magnetic particles per liposome (N_{p}) calculable as follows:

$$N_p = \frac{Q\,N_{ag}}{38\left(\dfrac{4\pi}{3}r_p^3\right)} \tag{3}$$

Then, by taking into account an average magnetic particle radius $r_{\text{p}} \approx 4$ nm,[28,46] one MFL unit of 200 nm in diameter was expected to entrap nearly 520 ± 60 maghemite nanocrystals.

Magnetic resonance (MR) relaxation behavior of water protons in the presence of MFLs in blood at the same magnetic field used for in vivo MR imaging is characterized by linear relationships between MFL concentration and the inverse of spin-lattice ($1/T_1$) and spin-spin ($1/T_2$) proton relaxation times. The slopes of the straight lines indicated significantly different longitudinal and transverse relaxivities $r_1 = 0.87 \pm 0.01 \times 10^{-3}$ M s^{-1} and $r_2 = 259.5 \pm 9.8 \times 10^{-3}$ M s^{-1}, respectively, leading to r_2/r_1 ratio close to 300 (Figure S1, Supporting Information). This result reflects large magnetic susceptibility in accordance with exceptional T_2-weighted MR contrast efficiency. As previously stated,[28,30] this arises from the confined state of the maghemite particles inside the liposome aqueous core so that each MFL unit behaves as a highly magnetizable particle which, once subjected to an external magnetic field, becomes able to locally produce a magnetic moment equivalent to the sum of the magnetic moments individually attributed to each encapsulated maghemite grain.

Maghemite nanoscale crystals, whether they are as free suspension or encapsulated in MFLs, displayed identical X-band electron spin resonance (ESR) spectra characterized by a broad line centered at a resonance field of 3227 ± 10 G ($g = 2.037$) with a line-width of 649 ± 24 G (Figure 1). Both free magnetic fluid and MFLs ESR spectra show a superimposed much narrower line noticeable at a larger field close to 3500 G and attributable to the smallest crystals forming the magnetic fluid.[47] The absence of any broadening or relative shift of the two ESR signal components when the maghemite grains were entrapped in the liposomes evidently supports that the physical state of the magnetic fluid was conserved within MFLs and no additional interparticle dipolar interactions, possibly due to partial aggregation, took place upon the encapsulation process.[48] Moreover, the area under the curve (AUC) of ESR signals measured from either free magnetic fluid or MFLs as a function of incremented Fe(III) concentrations indifferently depends on the iron oxide content according to a single linear relationship for both free and trapped maghemite grains thereby showing that unpaired electrons resonance absorption is not altered by intraliposome containment (Figure S2, Supporting Information).

2.2. In Vivo Magnetic Targeting of MFLs to Glioblastoma: Quantitative MRI Monitoring

Two groups of mice bearing human glioma U87 were intravenously injected with the same dose of MFLs and imaged by 7-T MRI, 4 h after administration, i.e., after a time period corresponding to a magnetic field gradient exposure previously stated as optimum for in vivo targeting conditions on the basis of characteristic circulation times of MFLs.[30] One group was subjected to an external 0.4-T magnet (190 T m^{-1} magnetic field gradient) placed onto the top of the head. T_2*-weighted 3D gradient echo (GE) sequences were implemented in order to best utilize the large magnetic susceptibility of MFLs. The magnetic fluid conveyed by MFLs is then visualized as hypointense signals seen on the MR images as darker regions due to the strong enhancement of the transverse magnetization decay rate of surrounding protons. **Figure 2** shows representative images obtained from MFL-injected mice either exposed to the magnet (Images A–C) or not (Images D–F). Prior to injection, glioblastoma location in the right brain hemisphere was specified by performing T_2-weighted spin echo (SE) acquisitions, which revealed malignant areas as hyper-intense lesions (Figure 2A,B) while no contrast could be detected by T_2*-weighted GE imaging (Figure 2B,E). Four hours after MFLs injection, the tumors belonging to the magnet-exposed animals were seen markedly dark (Figure 2C) whereas only a slight contrast was observed in the tumor region for the nontargeted group (Figure 2F). This clearly highlights the improvement of MFLs accumulation in glioblastoma under the influence of the magnetic filed gradient. The healthy cerebral areas of both brain hemispheres indifferently exposed to the magnet or not, do not exhibit significant signal reduction after injection except large blood vessels of pronounced hypointensity.

Confocal microscopy images shown in Figure 2 (Images G–J) explicitly point out the colocalization of the hypointense MR signals seen in brain of injected mice with the rhodamine-labeled vesicle structure of the magnetoliposomes. Especially higher fluorescence intensity is revealed at the magnetically targeted tumor site (Figure 2H,K) compared to the nontargeted one (Figure 2J,K). Observations by MRI and confocal microscopy strongly support that MFLs accumulate at the tumor site as intact structures.

In order to quantitatively assess the MR contrast due to MFLs accumulation in the tumor lesion through magnetic targeting, the relaxation rate of transverse magnetization ($R_2* = 1/T_2*$) either in glioblastoma or in contralateral brain area was determined from the signal intensity decay recorded versus echo

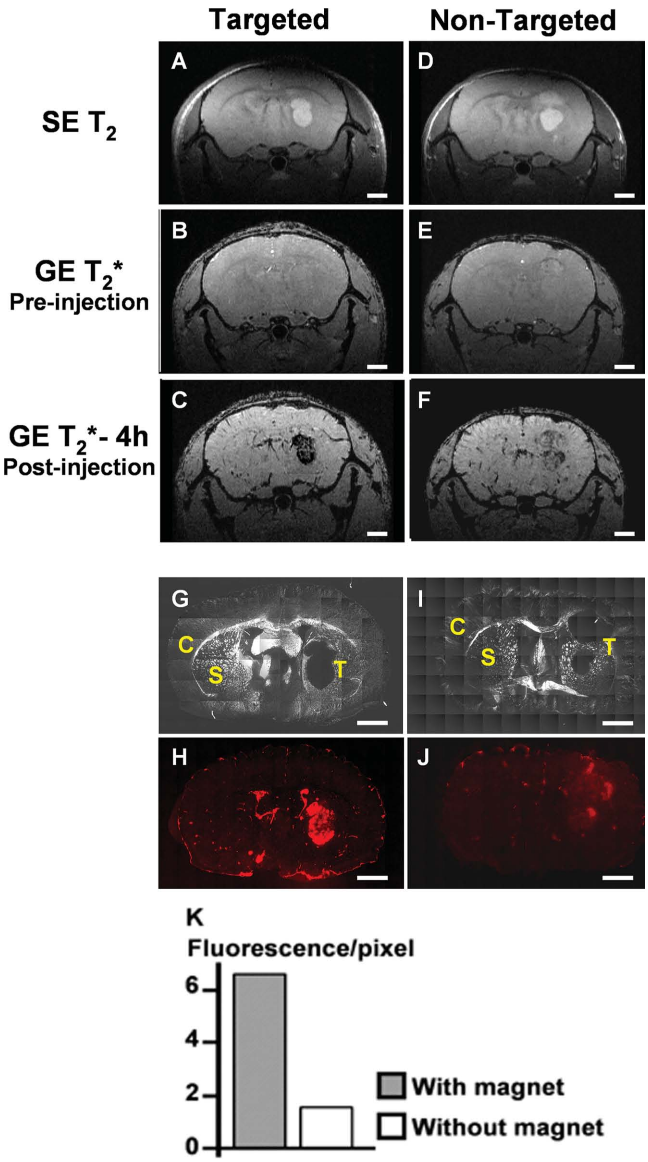

Figure 2. Representative in vivo 7-T MR images of intracerebral U87 glioblastoma in mice before and 4 h after intravenous injection of MFLs, with 0.4-T magnet-exposure (targeted group, left images A–C) or not (nontargeted group, right images D–F); the spin echo T_2-weighted (SE T_2) baseline acquisitions performed before MFLs injection (preinjection) show the tumor location clearly observable as a hyper-intense lesion (A,D); the T_2*-weighted 3D gradient echo (GE T_2*) sequences (B,E) recorded postinjection reveal the presence of MFLs in the tumors as hypointense contrast significantly much pronounced for the glioblastoma subjected to the magnet. G–J) The ex vivo confocal microscopy images of brain slices from the same mice as those imaged by MRI, show the fate of MFLs vesicle structure by revealing the fluorescence signal (in red) of the lipid label Rho-PE incorporated in the MFL membrane (excitation at 543 nm, collected emission LP 560nm); the tissue histology is shown by the bright field mosaic (with magnet, G; without magnet, I); graph K reports on Rho-PE fluorescence signal intensity in the tumor region (Supporting Information); rhodamine fluorescence areas due to the presence of MFLs appear significantly larger and of higher intensity for the targeted tumor; White bars represent 1 mm; C: cortex; S: striatum; T: tumor.

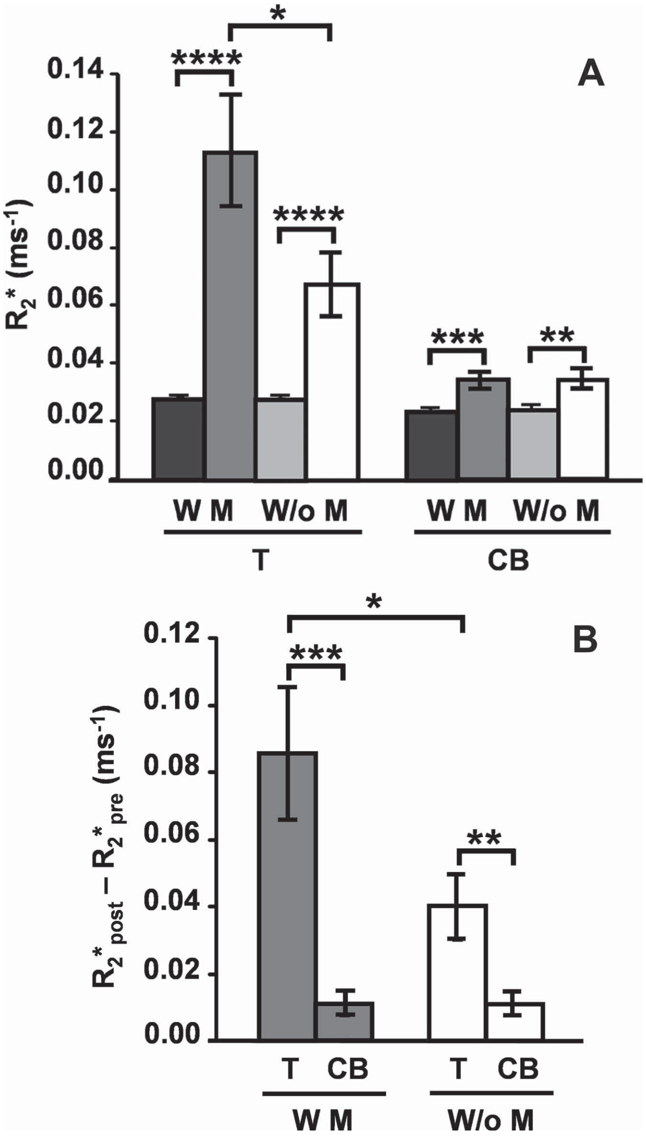

Figure 3. Efficiency versus selectivity evaluation by MRI of MFLs magnetic targeting towards glioblastoma. **A**) Relaxation rate (R_2*) in the tumor (T) and contralateral brain parenchyma (CB) before (left bar) and 4 h after (right bar) MFLs injection to mice either subjected to a 0.4-T magnet (WM, $n = 5$) for the same period of time or not (W/o M, $n = 5$). (**B**) Difference in relaxation rates determined 4 h after (R_2*post) and prior to (R_2*pre) MFLs injection for the two mice groups. Data are expressed as mean ± SD. Statistical analysis was performed using the bilateral unpaired Student's *t*-test: *$p < 0.005$, **$p < 0.001$, ***$p < 0.0001$, ****$p < 0.00005$.

time upon T_2*-weighted GE sequence acquisitions before and 4 h after MFL injection (**Figure 3**A). Before injection, the average relaxation rate attributed to the glioblastoma tissue was not significantly different between the two groups of mice, indicating that the intrinsic magnetic resonance behavior of the malignant lesions was uniform in all mice. Similarly, the relaxation rate in the contralateral healthy brain tissue was unchanged in all animals and differed very slightly from that determined in the tumor tissue. Hence, the changes in the R_2* value noticed after MFLs injection can only reflect the local concentration of the contrast agent in both brain regions. Four hours after MFLs injection to the mice not subjected to the magnetic field gradient, R_2* values in tumors and contralateral brain areas were found significantly increased compared to intrinsic relaxation of the tissues. This indicates that the contrast agent still circulated in brain 4 h postinjection in an amount properly perceptible by MRI, especially at the glioblastoma level (Figure 3A). In the case of mice with magnet, the contralateral response was the same as that determined for the group without magnet indicating that the magnetic field gradient did not induce additional MFLs accumulation in the healthy parenchyma. Contrariwise, R_2* in glioblastoma was substantially increased under magnetic field gradient, then demonstrating the effectiveness of magnetic targeting to enhance preferential accumulation of the contrast agent within the tumor. The gain of local MFLs concentration in a given tissue area can be more directly assessed by the difference between the relaxation rate determined post injection (overall contrast efficiency, $R_2^*{}_{post}$) and the relaxation rate measured prior to injection (endogenous response in the absence of contrast agent, $R_2^*{}_{pre}$). In other words, the increment in relaxation rate ($\Delta R_2^* = R_2^*{}_{post} - R_2^*{}_{pre}$) directly reflects the relaxivity behavior of the contrast agent in the tissues and is plausibly an increasing function of its local concentration.[24,49–51] Figure 3B displays the ($R_2^*{}_{post} - R_2^*{}_{pre}$) values corresponding to glioblastoma and contralateral brain areas, respectively, for mice either subjected to magnet exposure or not. By approximating similar relaxivity behaviors of the iron oxide within both intracerebral areas, the results indicate a selective increase in the contrast agent concentration at the tumor level beside the healthy brain parenchyma. This selective increase was moreover significantly emphasized by the magnet. Interestingly, no excess accumulation in the nonmalignant cerebral areas occurred upon magnetic targeting. ΔR_2* multiplying factors of 9 (with magnet) and 4 (without magnet) compared with healthy brain were measured, i.e., more than a twofold increase in the increment of relaxation rate.

Figure 4 shows the series of brain MR images acquired for a 24-h period after MFL injection for animals beforehand subjected to either 4-h magnetic targeting (Images A–H) or not (Images D–J). The hypointense signals seen at 4 h in the tumor region and cerebral vessels, more pronounced for the targeted tumor, decreased gradually with increasing time. However, significant persistence of the hyposignal at 8 h and 24 h was revealed in the magnet-exposed glioblastoma unlike in the nontargeted tumor. The difference in relaxation rates ($R_2^*{}_{post} - R_2^*{}_{pre}$) accounting for the local concentration in contrast agent (graph in Figure 4K) demonstrates the efficacy of the magnetic field-induced targeting. The remaining MR contrast due to contrast agent accumulation in glioblastoma 24 h postinjection was almost that reached in the absence of magnet 4 h postinjection.

2.3. Quantitative Ex Vivo ESR Analysis

Magnetic targeting effect on MFLs delivery to glioblastoma and biodistribution in major mononuclear phagocyte system (MPS) or clearing organs were independently assessed by ESR spectroscopy analysis of tissues excised after achieving animal

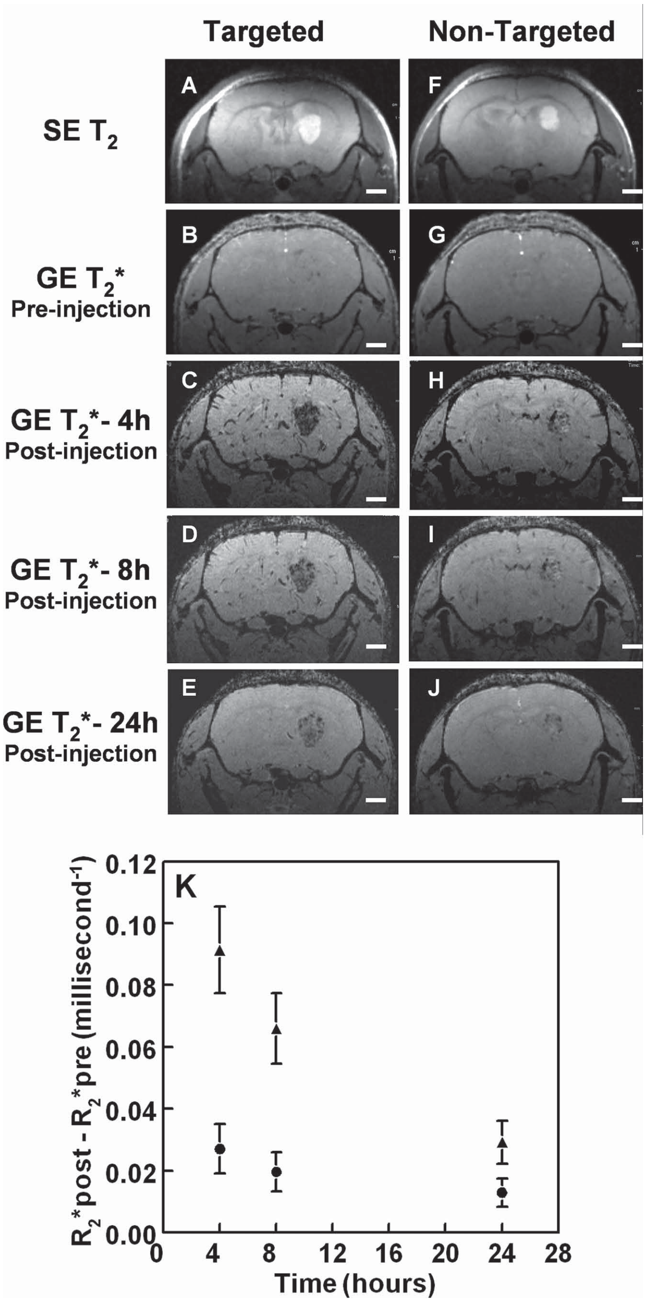

Figure 4. Series of brain MR images versus time from glioblastoma-bearing mice injected with MFLs and either subjected for 4 h postinjection to a 0.4-T magnet (A–E) or not (F–J); the spin echo T_2-weighted (SE T_2) baseline acquisitions performed before MFLs injection show the tumor locations as hyper-intense lesions (A,F); the T_2*-weighted gradient echo (GE T_2*) sequences reveal the presence of the contrast agent as hypointense areas (B–E, G–J); the persistence of the hyposignal at the targeted tumor level remains clearly visible 24 h postinjection (E). Relaxation rate difference ($R_2{}^*{}_{\text{post}} - R_2{}^*{}_{\text{pre}}$) for the targeted (▴) and nontargeted (•) tumors as a function of the time period following MFLs administration (K); the magnet was removed at 4 h for the targeted tumor. White bars represent 1 mm.

experiments based on the same conditions as those implemented for MRI monitoring. While preferential MFLs concentration was found in liver and spleen compared with kidneys and brain, this was not significantly affected by brain magnet-exposure (Figure S3, Supporting Information). Contrariwise, the amounts of iron oxide recovered within the whole brain including glioblastoma were found actually increased by magnetic targeting. The amount of iron oxide specifically delivered to the tumors versus normal brain parenchyma was determined from separate analyses of on one hand the upper quarter of the right brain hemisphere containing the whole glioblastoma and on the other hand the left healthy brain hemisphere. Given the mass fraction of the malignant lesion x in the tissue extract, the average content in magnetic material (µmol Fe(III)) per gram of tissue $C_{\text{FeIII}}{}^{\text{TUM}}$ delivered to glioblastoma was calculated according to the following equation:

$$C_{\text{FeIII}}^{\text{TUM}} = \left[C_{\text{FeIII}}^{\text{TOT}} - (1-x) C_{\text{FeIII}}^{\text{PAR}} \right] / x \tag{4}$$

where $C_{\text{FeIII}}{}^{\text{TOT}}$ is the total iron oxide concentration per unit mass of extract and $C_{\text{FeIII}}{}^{\text{PAR}}$ the iron oxide concentration per unit mass of normal brain parenchyma determined from left healthy brain hemispheres. Acceptable estimates of x values were deduced from glioblastoma volumes determined by T_2-weighted MRI by assuming tumor tissue density of 1g cm^{-3}.[52] This procedure worthily minimized the risk of error since the tumors were too small (volume < 8 µm^3) to be properly excised. Results for both groups of mice (**Figure 5**) show higher iron oxide concentrations in the tumors than those determined in normal brain, however in a much more emphasized manner for mice subjected to magnet influence. Iron accumulation in the whole malignant tissue corresponded to a concentration factor of 3.6 ± 1.7. This clearly points out the efficiency of magnetic targeting and its selectivity for glioblastoma, therefore confirming the conclusions supported by in vivo MRI monitoring.

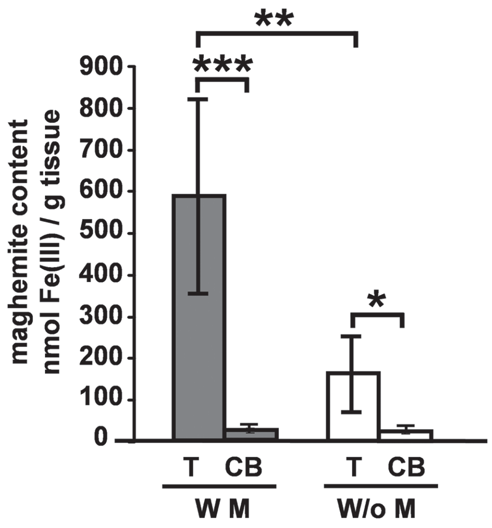

Figure 5. ESR analysis of iron oxide concentration (nanomoles of Fe(III) per unit mass of tissue) contained in either glioblastoma (T) or normal brain parenchyma (CB), 4 h after injection of MFLs to glioblastoma-bearing mice either subjected to a 0.4-T magnet (WM, $n = 5$) or not (W/o M, $n = 5$) at 12.8 µmol initial Iron(III) dose. Data are expressed as mean ± SD. Statistical analysis was performed according to the bilateral unpaired Student's t-test: $*p < 0.02$, $**p < 0.01$, $***p < 0.001$.

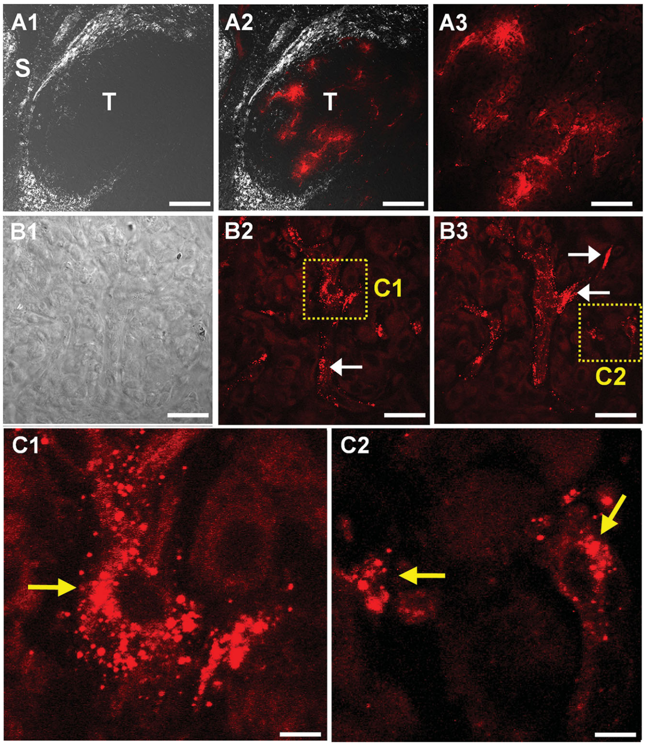

Figure 6. Confocal fluorescence microscopy images of glioblastoma tissue from mice injected with MFLs and subjected to a 0.4-T magnet for 4 h. Tissue histology is revealed by the bright field images. Rhodamine fluorescence associated with the structure of MFLs (excitation at 543 nm, collected emission LP 560 nm) is seen in red. Acquisitions: Plan Neofluar x10/0.3 (A1–A2, bar = 200 µm; T: tumor), Plan Apochromat 20× /0.75 (A3, bar = 100 µm), Plan Apochromat 63× /1.4NO oil (B1–B3, bar = 20 µm; C1–C2, bar = 5 µm) objective lens. The images reveal high concentrations of MFLs within the tumor, localized either in the vessels or extravascularly. Images (B2,B3) correspond to the same field of view with a 4.16-µm step along the *z*-axis while images (C1,C2) show higher magnifications of (B2) and (B3), respectively (areas delineated by dotted squares). MFLs are seen as small individual red spots within the vascular lumen (white arrows) and inside the cytoplasm of abluminal or tumor cells (yellow arrows).

2.4. Histological Analyses

Confocal fluorescence microscopy of brain glioblastoma slices from MFL-injected mice subjected for 4 h to the magnetic field gradient repeatedly showed highly intense rhodamine-fluorescence signals. These were concentrated in more or less extended delineated areas seen in red in the images and localized either within the microvasculature network or in the extravascular vicinity of blood capillaries (**Figure 6**, series A,B). High magnification of these areas revealed numerous red spots of size limited to a few pixels (0.14 × 0.14 μm^2 per pixel) undoubtedly compatible with the presence of MFL vesicular structures, some of them being clearly visible within intracellular compartments of either endothelial cells constituting the abluminal membrane or malignant glial cells (Figure 6, series C). Images of nontargeted tumor slices exhibited similar features but much more sparse, with moreover low-intensity rhodamine-fluorescence signals (data not shown).

Examination of magnetically targeted brain glioblastoma was performed at the cellular scale by transmission electron microscopy (TEM). The TEM images in **Figure 7** (Figures S4 and S5, Supporting Information) are representative of tumor slices devoid of vascular components by prior perfusion. The maghemite particles conveyed by MFLs are revealed as black nanoscale grains due to the high electron density of the iron atoms. They appear clustered in confined volumes with dimensions close to the initial diameter of the injected magnetoliposomes (Figure 1). Notoriously, no iron oxide traces could be seen in samples of the perfused contralateral hemispheres corresponding to healthy brain regions. Electron energy-loss spectroscopy (EELS) of TEM specimen confirmed that these structures are indeed made of iron oxide particles as exemplified by the EELS spectrum in Figure 7G showing transition peaks at the L_2 (Fe2$p_{1/2}\rightarrow$Fe3d, 718.8 eV) and L_3 (Fe2$p_{3/2}\rightarrow$Fe3d, 706 eV) edges of iron. Clusters of maghemite nanocrystals were clearly visualized inside cells lining the vascular lumen or in the adjacent extracellular matrix space (Figure 7A) suggesting that intracellular and possibly paracellular pathways were involved during MFLs extravasation. Similar clusters are also seen within the cytoplasm of malignant glial cells (Figure 7C) in agreement with intercellular or diffusion transport of MFLs within the interstitium. Interestingly, some clusters appeared to be concentrated within endosome-like structures (Figure 7B2,C2,C4,C5,D2), attributable to primary endocytotic vesicles containing MFL unit structures. This finding is consistent with the highly intense rhodamine-labeled vesicle-like patterns visualized within abluminal cells by confocal microscopy.

3. Discussion

The recurring difficulty in the use of lipid vesicles as carriers of materials encapsulated within their inner aqueous compartment is the distribution of the encapsulation rate inherent to the fabrication processes based on random trapping by bilayer membrane closure. Whereas sorting as a function of intravesicle loading is usually a tricky problem, it can be easily circumvented when the encapsulated material is magnetic. Thereby in this study, magnetic sorting of MFLs was performed to select the liposomes which responded to the same magnetic field gradient as that applied to mice brain tumors. This substantially standardized the intraliposome concentration in magnetic fluid and secured operational MFLs magnetic targeting. Final loading of 4.4 moles of Fe(III) per mole of lipids was checked and interestingly among the highest described ones for nanoscale magnetoliposomes entrapping an aqueous suspension of individualized iron oxide nanocrystals.[27,53–55] Cryo-TEM investigation accredited a perfectly spherical shape and enclosing by a regularly unilamellar membrane of the magnetoliposomes developed here. This reflects homogenous bilayer curvature and then uniform distribution of the different lipid components, especially ensuring uniform PEG brush coating[43] which is a prerequisite for optimizing in vivo stabilization and stealthiness of liposomes.[56–59]

The second major issue is to check that the whole vesicle structure of MFLs was preserved upon magnetic targeting. This

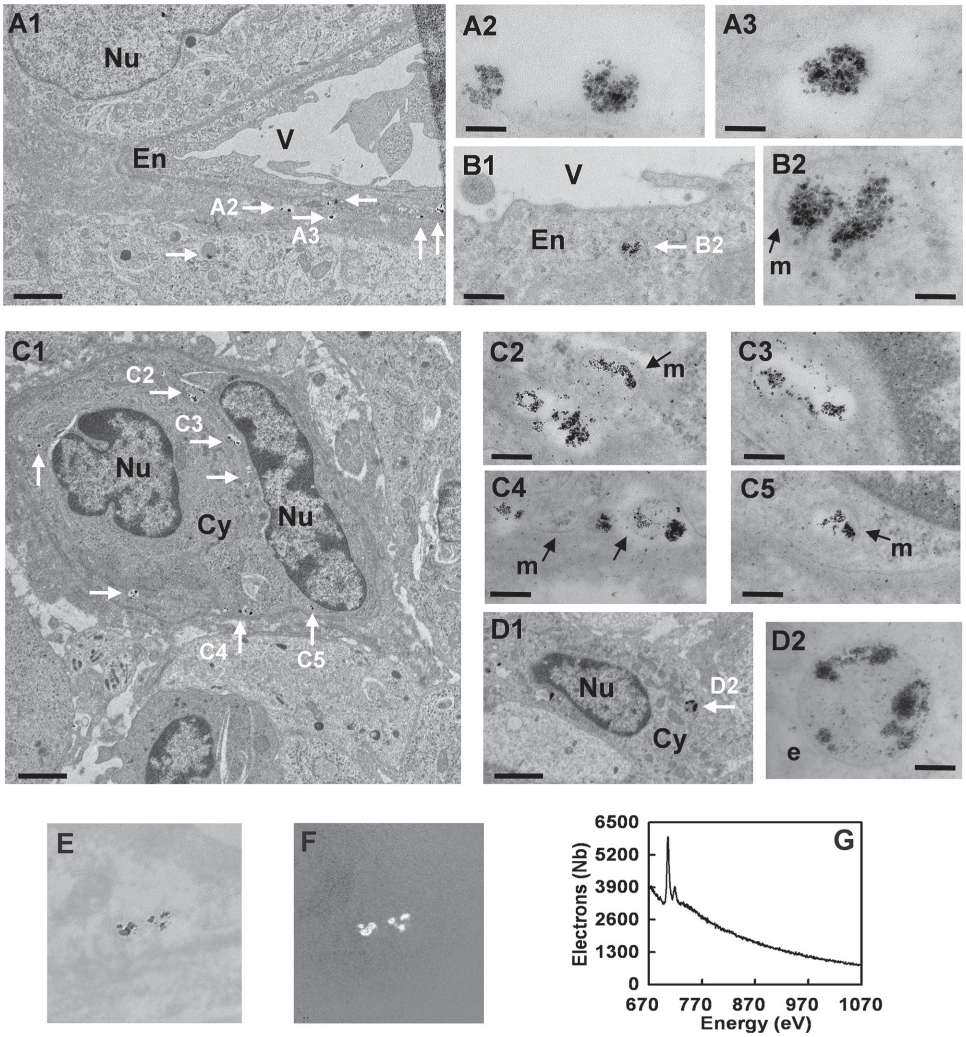

Figure 7. Transmission electron images of glioblastoma tissue from mice injected with MFLs and exposed to a 0.4-T magnet for 4 h; tissue perfusion was performed to eliminate vascular components. Iron oxide nanocrystals are observable as dark grains due to their high electron density (white arrows); images (A1, bar = 2 µm; A2-A3, bar = 100 nm; B1, bar = 0.5 µm; B2, bar = 100 nm) exemplify the location of iron oxide nanocrystals at the vicinity of a vessel (V) and seen gathered in small clusters with size close to that of initially injected MFLs (see Figure 1); images (C1, bar = 2 µm, C2-C5, bar = 200 nm; D1, bar = 2 µm; D2, bar = 100 nm) show similar clusters of iron oxide grains in tumor cells; some of the clusters are seen individually surrounded by a membrane (m, B2, C2, C4-C5) or included in an endosome-like structure (e, D2); Nu: nucleus; Cy: cytoplasm; En: endothelial cell. Identification of maghemite grains by energy filtered transmission electron microscopy (E–G); TEM image of dark spot clusters attributed to iron oxide grains (E); related electron spectroscopic iron mapping (F); electron energy-loss spectrum of the spots (G) revealing energy values corresponding to the electron transition from the 2p orbital to the 3d orbital (L_2 edge: 2p J = 1/2; L_3 edge: 2p J = 3/2) of Iron(III) in maghemite.

was achieved by double labeling of the core-shell structure. First, the fluorescent derivative Rho-PE was used to label the membrane shell of MFLs through a highly durable insertion within the phospholipid bilayer. This probe is indeed reliably stable in biological fluids and does not exchange with plasma proteins.[60,61] As already been widely tried out, Rho-PE accurately reports MFLs in blood vessels, living cells or tissue specimen as very intense fluorescent concentrates of small individual spots the emission signal of which is not affected by the presence of maghemite nanocrystals.[29,31–33,35,53] Secondly, the encapsulated magnetic fluid intrinsically provides an excellent tracking tool of the intraliposome compartment by MR Imaging and ESR spectrometry which both exploit magnetic resonance phenomena generated by the superparamagnetic behavior of the iron oxide nanocrystals. MRI relies on the high magnetic susceptibility of MFLs which indeed confine lots of maghemite grains. This strongly enhances proton spin–spin relaxation as demonstrated by the outstanding value of transverse relaxivity found here for MFLs in blood at 7-T magnetic field. The spatial location of iron oxide is therefore indirectly detected by the shortening of the transverse relaxation times of the surrounding water protons which results as a significant reduction of the signal intensity seen as a negative contrast on the MR images.[62–66] In this respect, T_2*-weighted GE sequences can be advantageously privileged to emphasize local susceptibility effects on proton T_2-decay rates expected particularly significant in the vicinity of MFLs. Besides, ESR spectrometry provides direct determination of amounts of paramagnetic species, here given by the energy absorption from a 9.72-GHz radiofrequency microwave by the unpaired electrons contained in the maghemite nanocrystals. The ESR response primarily and quantitatively depends on the number and intrinsic structure of the iron(III) oxide molecules as well as on the size of the assemblies they form.[24,43,67–70] Moreover, iron oxide particles are inherently excellent contrast agent for transmission electron microscopy allowing their direct identification on the TEM images from tissue samples.

The undeniable advantage of MRI is its usefulness to achieve in vivo noninvasive monitoring of MFLs. Our results ascertained its effectiveness not only to point out the presence of the contrast agent in vivo but also to assess its local concentration through proton relaxation rate measurements. This is based on the explicit agreement between the quantitative MRI data and the independent ESR measurement of the iron oxide contents in normal brain versus glioblastoma tissues. Such quantitative MRI monitoring had been successfully practiced to track magnetic particles in vivo in glioma-bearing rats,[24,71] but not yet utilized with magnetoliposome systems until the present study. To go further in this methodology, it is worth noting that the magnetic targeting index found in this study, i.e., the ratio of the two accumulation rates obtained with and without magnet, respectively, reached 2.2 from MRI monitoring against 3.6 by ESR analysis. In fact, while ESR amounts the total maghemite content per biological extract in its whole, the proton relaxation rate R_2* reflects the local concentration effect of MFLs or maghemite particles (i.e., the relative proportion of contrast agent to water protons in the imaged tissue) with a local dose-response affected by the nature of the surrounding medium. In this respect, it has been theoretically predicted and experimentally verified that the proton spin-spin relaxation due to a magnetic susceptibility effect in tissue interstitium linearly increases with increasing the concentration in contrast agents, while a quadratic response is expected in blood.[72] Therefore, according to the hypothesis supported by the 24-h release experiment, that the magnetic force caused an improved retention effect within the glioblastoma tissue compared with nontargeted conditions in which MFL concentration likely remained preferentially vascular, the R_2*-based magnetic targeting index may underestimate the effective gain in local contrast agent concentration. Conversely, as ESR analysis gave the actual iron oxide amounts contained in the regions of interest and acted as a robust reference, the difference noticed between ESR assessment and MRI results may suggest that magnetic targeting of MFLs actually changes their local distribution in glioblastoma.

Taken together, the different approaches implemented in this work to independently account for the fates of inner iron oxide content and lipid vesicle shell converged on the nonambiguous conclusion that the magnetoliposomes were delivered in glioblastoma via the vasculature and as intact structures. This fully agrees with previously demonstrated intravascular behavior of MFLs indeed shown to circulate in blood flow without structural damage and loss of encapsulation material.[29] Typically in glioblastoma, perfect superimposition of Rho-PE fluorescence from ex vivo confocal microscopy and areas of pronounced negative signal in MR images obtained on the same animal (Figure 2) demonstrates colocalization of vesicle lipid bilayer and concentrated iron oxide which can only be explained by the presence of entire MFLs. Ascertainment of pronounced MRI negative contrast 4 h after MFLs injection to mice subjected to a magnet or, to some extent without magnet, also supports the conservation of the intraliposome containment state of the magnetic fluid. As a matter of fact, the presence of the magnetic field gradient significantly enhanced MFLs concentration within the tumors. Histological investigations clearly revealed vascular accumulation of the magnetoliposomes in the malignant lesion beside partial extravasation and uptake by the malignant glial cells afterwards their passage through the abluminal membrane. Extravasation pathway of MFLs was indeed expected and made possible by structural abnormalities of the endothelial lining of glioma microvasculature which have been well shown as factors of permeability to colloidal systems.[6–8,73,74] TEM images of perfused glioblastoma (Figure 7) underscored clusters of iron oxide particles, each of them likely having one MFL structure as precursor and traced within the cytoplasm of endothelial cells or in the interstitium suggesting vesicular transport and trans/intercellular diffusion processes already identified as consequences of tumor angiogenesis.[14,75] These findings strongly support that a part of MFLs were subjected to EPR effect. In this respect, the time-course experiment summarized by Figure 4 deserves special attention. For mice subjected to a 4-h magnet exposure, the proton relaxation rates measured 8 h and 24 h after injection remained clearly higher than those found in the absence of magnetic field gradient. Especially, the R_2* increment at 24 h for the magnet-exposed glioblastoma was close to that found 4 h after injection for the nontargeted tumor. These observations indicate that the magnetic field gradient enhanced the local accumulation of the contrast agent in a manner that the accumulated MFL amount was significantly retained versus time at the tumor level despite magnet removal. This clearly underlines a nonnegligible tumor clearance according to an enhanced permeation and retention effect. Indeed, if MFLs accumulation in the tumor during the 4-h magnet-exposure period was limited to the intravascular compartment, stopping magnetic field gradient would release the retained magnetoliposomes in whole bloodstream similarly to a second MFLs injection. Then, the resulting plasmatic concentration reflected by MRI at glioblastoma level should reach that observed without magnet at the same time period or very nearly according to the first-order kinetics (monoexponential decay) of MFL plasmatic concentration.[29] This was obviously not the case. At this stage of knowledge, further investigations would deserve to be undertaken in order to securely confirm the influence of magnetic targeting on the time-course of intratumor magnetoliposome concentration. In other words, the question which could be especially addressed is whether maintaining high intravascular MFLs concentrations in glioblastoma by pursuing magnetic field gradient application for periods of time longer than 4 h, may increase the amount of MFLs delivered in the tumor interstitium or not. Indeed, whereas a 4-h exposure to a magnetic field gradient had reliably been shown to allow optimal intravascular concentration effect of MFLs in malignant lesions,[30] the results obtained here do not exclude that extravasation of the magnetoliposomes is a slower process since a part of the accumulated magnetoliposomes was released upon magnet removal as depicted by decrease in R_2* increment.

The efficacy of magnetic targeting to concentrate MFLs in glioblastoma is reinforced by the selective accumulation of MFLs in the tumor lesion compared to healthy brain parenchyma, indeed spared from the influence of the magnetic field gradient as shown by both MRI monitoring and ESR spectrometry as well as by TEM that did not reveal any iron oxide traces in perfused contralateral brain samples. This result deserves a comment regarding one of our pioneering studies which has demonstrated an effect of local and reversible vascular concentration of MFLs in the meningeal and superficial cortical venules of mice brain under the direct influence of a 0.1-T magnet.[53] These observations were made by video microscopy at a depth of 0.2 µm from the magnet in direct contact with a cranial window surgically placed onto the animal brain cortex. The accumulation of MFLs occurred only at the very vicinity of the magnet. The present work demonstrates that the contribution of such a superficial vascular concentration effect is negligible compared to the whole brain and then agrees with our previous statements that neither arterioles nor deep venules are subjected to magnetoliposomes accumulation. It had been moreover shown that this phenomenon did not affect cerebral blood flow and was perfectly reversible after magnet removal.[53] We can reasonably anticipate that magnetic targeting of glioblastoma can be adjustable in order to avoid cerebrovascular accidents or local hypoxia of the healthy brain regions. On the other hand, MFLs circulate as intact structures in blood compartment. This guarantees no leakage of free maghemite grains since the magnetoliposomes unit size obviously impedes their passage through healthy blood-brain barrier due to its outstandingly low permeability.[2,3]

MFLs magnetic targeting selectivity towards glioblastoma originates from preferential accumulation in the microvasculature of the tumor lesion. This mechanism agrees with earlier works[30–32] and was substantiated in this study. A plausible explanation of magnetically induced accumulation may be that the magnetic force experienced by MFLs would be sufficient to offset the hydrodynamic drag force in the direction of blood flow. An estimate of the magnetic force F_m exerted onto MFLs by the 0.4-T magnet (magnetic field gradient $\mathrm{grad}B = 190\ \mathrm{T\ m^{-1}}$) used here for magnetic sorting and in vivo targeting, can be calculated as:[33,53]

$$F_\mathrm{m} = N_\mathrm{p}\, m_\mathrm{eff}\, \mathrm{grad}B \quad (5)$$

According to Equation (4), one magnetoliposome of 200 nm in hydrodynamic diameter ($r_\mathrm{h} = 100$ nm) which entraps 560 maghemite nanoparticles ($N_\mathrm{p} = 560$, see result section) of effective magnetic moment $m_\mathrm{eff} \approx 1.4 \times 10^{-19}$ A m per particle,[28,33,76] is subjected to a magnetic force close to $F_\mathrm{m} = 1.5 \times 10^{-14}$ N. On the other hand, by applying Stokes' law for spherical particles, the hydrodynamic force exerted onto the magnetoliposomes is given by:

$$F_\mathrm{h} = 6\pi r_\mathrm{h} \eta v \quad (6)$$

where η ($\approx 3\ 10^{-3}$ Pa s) and v are blood viscosity and velocity, respectively. Blood velocity is related to blood flow rate, vessels section and density, which all differ between normal brain and high-grade glioma lesions. On the basis of experiments performed on rats or mice, the blood flow rate in cerebral tumors can be decreased by about 30–40% compared to normal brain.[23,77] and capillary diameter mainly ranges from 3 to 40 µm, i.e., nearly 3–5 times larger than healthy cerebral microvasculature.[7,23] Taking average capillary flow rates of 7.4×10^{-4} m s^{-1} and 3.1×10^{-3} m s^{-1} in tumor lesion and in normal brain region, respectively checked from 9L-glioma-bearing rats,[23] the hydrodynamic drag force F_h reaches estimated values of 4.2×10^{-12} N in tumor microvasculature against 1.7×10^{-11} N in normal brain. Despite reduction in glioma capillaries, the driving force in blood flow remains hundred times greater than the magnetic force and then cannot explain selective MFLs accumulation in tumor vasculature. As previously discussed,[30,31,53] gradual concentration of the magnetoliposomes is only possible because of their dipole-dipole interaction forces which develop in a continuous magnetic field with a magnitude around 10^{-12} N for two interacting MFLs.[53] MFLs mutual attraction is indeed able to balance the hydrodynamic drag force and rightly governs cluster formation in glioblastoma vasculature. To a certain extent, dipole–dipole attraction could remain insufficient to stop MFLs in normal brain vasculature regarding the F_h value about ten times greater. Nevertheless, to form a cluster, it is necessary to first immobilize some of the magnetoliposomes which then serves as initiators. This may occur owing to the heterogeneous glioma angio-architecture characterized by tortuous, dilated vessel loops and a lot of anarchical connections which may significantly and transiently slow down blood flow rate in some localized places where the largest and then the more magnetic MFLs could be arrested, while it is prominently not the case in healthy cerebral vessels.[7,78] That said, by assuming a Poiseuille flow regime, it cannot be ruled out that the rate of the magnetoliposomes is significantly slowed down at the wall of the vessels, thereby creating possible sites of accumulation. This can occur in the tumor and non-tumor regions. However, our results showed that this phenomenon is fully reversible and that the subsequent accumulation of circulating liposomes driven in the middle of the blood vessels is significantly limited even negligible in the healthy brain compared to the tumor region. Another hypothesis may be that interactions with microvascular endothelium during the earlier steps of extravasation can contribute to immobilize some magnetoliposomes for a sufficiently long time at the luminal/abluminal interface to favor dipole–dipole attraction while such interactions are inexistent in normal BBB. Anyway, the different results shown in this study undoubtedly demonstrate that, once extravasation achieved by EPR effect, the magnetic force efficiently acts to retain MFLs in the tumor interstitium and leads to their internalization by the malignant cells.

4. Conclusions

This work as a whole legitimates the potential of the superparamagnetic PEG-ylated liposomes developed here to magnetically target glioblastoma. Although they do not escape to MPS or clearing organs, especially to hepatic clearance, like the majority of magnetic colloids (Cole 2011),[69] their responsiveness to a magnetic field gradient and their robustness since they circulate as intact structures, provide a potent tool to selectively reach the cerebral tumor lesions by enhanced EPR effect while totally sparing healthy brain. This makes MFLs potent delivery systems of therapeutic molecules which can be trapped inside the aqueous volume of the liposomes or incorporated in their lipid membrane. The carried magnetic fluid which remains locally concentrated until cell internalization allows an additional opening in glioblastoma treatment by implementing localized hyperthermia controlled by the application of an alternative magnetic field.[27,79–83] At last, quantitative MR imaging was here warranted as an efficient noninvasive method to assess both localization and amount increment of delivered magnetoliposomes and will be used to investigate the time-course of MFLs by varying magnetic targeting parameters in order to optimize the enhancement of intraglioblastoma retention.

Supporting Information

Supporting Information is available from the Wiley Online Library or from the author.

Acknowledgements

This work was supported by a grant of the French Ministry of Research. The authors gratefully thank P. Legras and all the staff of the Angers Animal Facility SCAHU for assistance with the animals, V. Domergue-Dupont (Plateforme Animex, IFR141, Université Paris-Sud) and D. David (Laboratoire de Neuropharmacologie des Troubles Anxio-Dépressifs et Neurogenèse, EA 3544, Université Paris-Sud) for advice and help in histology experiments, A. Michel (Laboratoire Phenix, UMR CNRS 8234, Université Pierre et Marie Curie – Paris VI) for atomic absorption analysis, C. Sebrie (Laboratoire d'Imagerie par resonance magnétique Médicale et Multi-modalités IR4M, UMR CNRS 8081, Université Paris-Sud) for convenient access to a MRI workstation and computational image analysis tools and P. Gonin, C. Laplace, V. Rouffiac (Institut Gustave Roussy, France) for help in complementary in vivo fluorescence imaging investigations.

Received: July 10, 2014
Revised: October 1, 2014
Published online: January 14, 2015

[1] E. A. Neuwelt, M. Glasberg, E. Frenkel, P. Barnett, *Ann. Neurol.* **1984**, *14*, 316.
[2] N. J. Abbott, A. A. K. Patabendige, D. E. M. Dolman, S. R. Yusof, D. J. Begley, *Neurobiol. Dis.* **2010**, *37*, 13.
[3] Y. Omidi, J. Barar, *Bioimpacts* **2012**, *2*, 5.
[4] B. Pavan, A. Dalpiaz, N. Ciliberti, C. Biondi, S. Manfredini, S. Vertuani, *Molecules* **2008**, *13*, 1035.
[5] W. M. Pardridge, *Bioconjugate Chem.* **2008**, *19*, 1327.
[6] S. Liebner, A. Fischmann, G. Rascher, F. Duffner, E. H. Grote, H. Kalbacher, H. Wolburg, *Acta Neuropathol.* **2000**, *100*, 323.
[7] P. Vajkoczy, M. D. Menger, *J. Neuro-oncol.* **2000**, *50*, 99.
[8] D. C. Davies, *J. Anat.* **2002**, *200*, 639.
[9] M. C. Papadopoulos, S. Saadoun, D. K. Binder, G. T. Manley, S. Krishna, A. S. Verkman, *Neuroscience* **2004**, *129*, 1011.
[10] Y.-E. L. Koo, G. R. Reddy, M. Bhojani, R. Schneider, M. A. Philbert, A. Rehemtulla, B. D. Ross, R. Kopelman, *Adv. Drug Delivery Rev.* **2006**, *58*, 1556.
[11] G. Orive, O. A. Ali, E. Anitua, J. L. Pedraz, D. F. Emerich, *Biochim. Biophys. Acta* **2010**, *1806*, 96.
[12] G. Caruso, M. Caffo, C. Alafaci, G. Raudino, D. Cafarella, S. Lucerna, F. M. Salpietro, F. Tomasello, *Nanomedicine* **2011**, *7*, 744.
[13] N. Y. Hernandez-Pedro, E. Rangel-Lopez, R. Magana-Maldonado, V. Perez de la Cryz, A. Santamaria del Angel, B. Pineda, J. Sotelo, *Biomed. Res. Int.* **2013**, *2013*, 351031.
[14] H. Maeda, *Adv. Enzyme Regul.* **2001**, *41*, 189.
[15] A. Béduneau, P. Saulnier, J. P. Benoit, *Biomaterials* **2007**, *28*, 4947.
[16] Y. Zhang, Y. F. Zhang, J. Bryant, A. Charles, R. J. Boado, W. M. Pardridge, *Clin. Cancer Res.* **2004**, *10*, 3667.
[17] C. Sun, O. Veiseh, J. Gunn, C. Fang, S. Hansen, D. Lee, R. Sze, R. G. Ellenbogen, J. Olson, M. Zhang, *Small* **2008**, *4*, 372.
[18] B. Feng, K. Tomizawa, H. Michiue, S.-I. Miyatake, X.-J. Han, A. Fujimura, M. Seno, M. Kirihata, H. Matsui, *Biomaterials* **2009**, *30*, 1764.
[19] H. Xie, Y. Zhu, W. Jiang, Q. Zhou, H. Yang, N. Gu, Y. Zhang, H. Xu, X. Yang, *Biomaterials* **2011**, *32*, 495.
[20] H. Yan, J. Wang, P. Yi, H. Lei, C. Zhan, C. Xie, L. Feng, Q. Jun, J. Zhu, W. Lu, C. Li, *Chem. Commun.* **2011**, *47*, 8130.
[21] V. P. Chekhonin, V. Baklaushev, G. M. Yusubalieva, A. E. Belorusova, M. V. Gulyaev, E. B. Tsitrin, N. F. Grinenko, O. I. Gurina, Y. A. Pirogov, *Nanomedicine* **2012**, *8*, 63.
[22] S. K. Pulfer, S. L. Ciccotto, M. Gallo, *J. Neuro-oncol.* **1999**, *41*, 99.
[23] B. Chertok, A. E. David, Y. Huang, V. C. Yang, *J. Controlled Release* **2007**, *122*, 315.
[24] B. Chertok, B. A. Moffat, A. E. David, F. Yu, C. Bergemann, B. D. Ross, V. C. Yang, *Biomaterials* **2008**, *29*, 487.
[25] J. Q. Zhang, Z. R. Zhang, H. Yang, Q. Y. Tan, S. R. Qin, X. L. Qiu, *Pharm. Res.* **2005**, *22*, 573.
[26] J. P. Fortin-Ripoche, M. S. Martina, F. Gazeau, C. Ménager, C. Wilhelm, J. C. Bacri, S. Lesieur, O. Clément, *Radiology* **2006**, *239*, 415.
[27] S. J. H. Soenen, M. Hodenius, M. De Cuyper, *Nanomedicine* **2009**, *4*, 177.
[28] V. Plassat, C. Wilhelm, V. Marsaud, C. Ménager, F. Gazeau, J. M. Renoir, S. Lesieur, *Adv. Funct. Mater.* **2011**, *21*, 83.
[29] V. Plassat, J. M. Renoir, G. Autret, V. Marsaud, C. Ménager, O. Clément, S. Lesieur, *J. Bioanal. Biomed.* **2013**, *5*, 28.
[30] H. Marie, V. Plassat, S. Lesieur, *J. Drug Delivery Sci. Technol.* **2013**, *23*, 25.
[31] M. S. Martina, J. P. Fortin-Ripoche, C. Ménager, O. Clément, G. Barratt, C. Grabielle-Madelmont, F. Gazeau, V. Cabuil, S. Lesieur, *J. Am. Chem. Soc.* **2005**, *127*, 10676.
[32] V. Plassat, M. S. Martina, G. Barratt, C. Ménager, S. Lesieur, *Int. J. Pharm.* **2007**, *344*, 118.
[33] M. S. Martina, J. P. Fortin-Ripoche, L. Fournier, C. Ménager, F. Gazeau, O. Clément, S. Lesieur, *Mol. Imaging* **2007**, *6*, 140.
[34] M. S. Martina, V. Nicolas, C. Wihelm, C. Ménager, G. Barratt, S. Lesieur, *Biomaterials* **2007**, *28*, 4143.
[35] M S. Martina, C. Wihelm, S. Lesieur, *Biomaterials* **2008**, *29*, 4137.
[36] R. Stupp, W. P. Mason, M. J. van den Bent, M. Weller, B. Fisher, M. J. B. Taphoorn, K. Belanger, A. A. Brandes, C. Marosi, U. Bogdahn, J. Curschmann, R. C. Janzer, S. K. Ludwin, T. Gotlia, A. Allgeier, D. Lacombe, J. G. Cairncross, E. Eisenhauer, R. O. Mirimanoff, *N. Engl. J. Med.* **2005**, *352*, 987.
[37] V. Laquintana, A. Trapani, N. Denora, F. Wang, J. M. Gallo, G. Trapani, *Expert Opin. Drug Delivery* **2009**, *6*, 1017.
[38] M. M. Mrugala, *Discovery Med.* **2013**, *15*, 221.
[39] S. Lesieur, C. Grabielle-Madelmont, C. Ménager, V. Cabuil, D. Dadhi, P. Pierrot, K. Edwards, *J. Am. Chem. Soc.* **2003**, *125*, 5266.
[40] D. D. Lasic, D. Needham, *Chem. Rev.* **1995**, *95*, 2601.
[41] A. K. Kenworthy, K. Hristova, D. Needham, T. J. Mcintosh, *Biophys. J.* **1995**, *68*, 1921.
[42] P. G. De Gennes, *Macromolecules* **1980**, *13*,1069.

[43] S. Beugin, K. Edwards, G. Karlsson, M. Ollivon, S. Lesieur, *Biophys. J.* **1998**, *74*, 3196.
[44] D. Small, The physical chemistry of lipids: from alkanes to phospholipids. *Handbook of lipid research*Plenum Press, New York **1986**, Ch. 12, p. 512.
[45] H. I. Petrache, S. Tristam-Nagle, J. F. Nagle, *Chem. Phys. Lipids* **1998**, *95*, 83.
[46] C. Wilhelm, F. Gazeau, J. C. Bacri, *Eur. Biophys. J.* **2002**, *31*, 118.
[47] F. Gazeau, V. Shilov, J. C. Bacri, E. Dubois, F. Gendron, R. Perzynski, Y. L. Raikher, V. I. Stepanov, *J. Magn. Magn. Mater.* **1999**, *202*, 535.
[48] M. M. Noginov, N. Noginova, O. Amponsah, R. Bah, R. Rakhimov, V. A. Atsarkin, *J. Magn. Magn. Mater.* **2008**, *320*, 2228.
[49] L. Ostergaard, *J. Magn. Reson. Imaging* **2005**, *22*, 710.
[50] C. Z. Simonsen, L. Ostergaard, P. Verstergaard-Poulsen, L. Rohl, A Bjørnerud, C. Gyldensted, *J. Magn. Reson. Imaging* **1999**, *9*, 342.
[51] R. M. Weisskoff, C. S. Zuo, J. L. Boxerman, B. R. Rosen, *Magn. Reson. Med.* **1994**, *31*, 601.
[52] G. R. DiResta, J. Lee, N. Lau, F. Ali, J. H. Galicich, E. Arbit, *Acta Neurochir.* **1990**, *Suppl 51*, 34.
[53] C. Rivière, M. S. Martina, Y. Tomita, C. Wilhelm, A. Tran Dinh, C. Ménager, E. Pinard, S. Lesieur, F. Gazeau, J. Seylaz, *Radiology* **2007**, *244*, 439
[54] B. Garnier, S. Tan, S. Miraux, E. Bled, A. R. Brisson, *Contrast Media Mol. Imaging* **2012**, *7*, 231.
[55] G. Bealle, R. Di Corato, J. Kolosnjaj-Tabi, V. Dupuis, O. Clément, F. Gazeau, C. Wilhelm, C. Ménager, *Langmuir* **2012**, *28*, 11834.
[56] G. Gregoriadis, A. T. Florence, *Cancer Cells* **1991**, *3*, 144.
[57] D. Needham, K. Hristova, T. J. McIntosh, M. Dewhirst, N. Wu, D. D. Lasic, *J. Liposome Res.* **1992**, *2*, 411.
[58] T. M. Allen, C. B. Hansen, D. E L. de Menezes, *Adv. Drug Delivery Rev.* **1995**, *16*, 267.
[59] M. C. Woodle, *Adv. Drug Delivery Rev.* **1998**, *32*, 139.
[60] S. W. Davidson, A. B. Ghering, L. Beish, M. R. Tubb, D. Y. Hui, K. Pearson, *J. Lipid Res.* **2006**, *47*, 440.
[61] V. P. Torchilin, *Adv. Drug Delivery Rev.* **2005**, *57*, 95.
[62] P. Mowat, F. Franconi, C. Chapon, L. Lemaire, J. Dorat, F. Hindre, J. P. Benoît, P. Richomme, *NMR Biomed.* **2007**, *20*, 21.
[63] R. Weissleder, *Eur. Radiol.* **1993**, *3*, 198.
[64] C. Corot, P. Robert, J.-M. Idee, M. Port, *Adv. Drug Delivery Rev.* **2006**, *58*, 1471.
[65] Y.-X. J. Wang, *Eur. Radiol.* **2001**, *11*, 2319.
[66] Y.-X. J. Wang, *Quant. Imaging Med. Surg.* **2011**, *1*, 35.
[67] B. Chertok, A. J. Cole, A. E. David, V. C. Yang, *Mol. Pharm.* **2010**, *7*, 375.
[68] B. Chertok, A. E. David, V. C. Yang, *J. Controlled Release* **2011**, *155*, 393.
[69] A. J. Cole, A. E. David, J. Wang, C. J. Galban, V. C. Yang, *Biomaterials* **2011**, *32*, 6291.
[70] M. Levy, N. Luciani, D. Alloyeau, D. Elgrabli, V. Deveaux, C. Pechoux, S. Chat, G. Wang, N. Vats, F. Gendron, C. Factor, S. Lotersztajn, A. Luciani, C. Wilhelm, F. Gazeau, *Biomaterials* **2011**, *32*, 3988.
[71] M.-Y. Hua, H.-L. Liu, H.-W. Yang, P.-Y. Chen, R.-Y. Tsai, C.-Y. Huang, I-C. Tseng, L.-A. Lyu, C.-C. Ma, H.-J. Tang, T.-C. Yen, K.-C. Wei, *Biomaterials* **2011**, *32*, 516.
[72] A. Bjørnerud, FYS-KJM 4740, *The physics of MRI* **2008**, Ch. 11, pp. 129–144.
[73] S. Shibata, *Acta Neuropathol.* **1989**, *78*, 561.
[74] H. N. On, R. Mitchell, S. D. Savant, C. J. Bachmeier, G. H. Hatch, D. W. Miller, *J. Neuro-oncol.* **2012**, *117*, 204.
[75] Y. Matsumura, H. Maeda, *Cancer Res.* **1986**, *46*, 6387.
[76] P. Smirnov, F. Gazeau, M. Lewin, J. C. Bacri, N. Siauve, C. Vayssettes, C. A. Cuenod, O. Clement, *Magn. Res. Med.* **2004**, *52*, 73.
[77] D. R. Groothuis, J. F. Pasternak, J. M. Fischer, R. G. Blasberg, D. D. Bigner, N. A. Vick, *Cancer Res.* **1983**, *43*, 3362.
[78] S. Bulnes, J. Bilbao, J. V. Lafuente, *Histol. Histopathol.* **2009**, *24*, 693.
[79] A. Jordan, R. Scholz, P. Wust, H. Fähling, R. Felix, *J. Magn. Magn. Mater.* **1999**, *201*, 413.
[80] J. P. Fortin-Ripoche, F. Gazeau, C. Wilhelm, *Eur. Biophys. J.* **2008**, *37*, 223.
[81] A. Ito, M. Shinkai, H. Honda, T. Kobayashi, *J. Biosci. Bioeng.* **2005**, *100*, 1.
[82] K. Maier-Hauff, R. Rothe, R. Scholz, U. Gneveckow, P. Wust, B. Thiesen, A. Feussner, A. von Deimling, N. Waldoefner, R. Felix, A. Jordan, *J. Neuro-oncol.* **2007**, *81*, 53.
[83] K. Maier-Hauff, F. Ulrich, D. Nestler, H. Niehoff, P. Wust, B. Thiesen, H. Orawa, V. Budach, A. Jordan, *J. Neuro-oncol.* **2011**, *103*, 317.